Fourier optics of image formation in LEEM

2009 J. Phys.: Condens. Matter 21 314006

(http://iopscience.iop.org/0953-8984/21/31/314006)

J. Phys.: Condens. Matter **21** (2009) 314006 (10pp) doi:10.1088/0953-8984/21/31/314006

Fourier optics of image formation in LEEM

A B Pang[1], Th Müller[2], M S Altman[1] and Ernst Bauer[2]

[1] Department of Physics, Hong Kong University of Science and Technology, Clear Water Bay, Kowloon, Hong Kong
[2] Physikalisches Institute, Technische Universität Clausthal, Leibnizstrasse 4, D-38678 Clausthal-Zellerfeld, Germany

Received 19 December 2008
Published 7 July 2009
Online at stacks.iop.org/JPhysCM/21/314006

Abstract
A Fourier optics calculation of image formation in low energy electron microscopy (LEEM) is presented. The adaptation of the existing theory for transmission electron microscopy to the treatment of LEEM and other forms of cathode lens electron microscopy is explained. The calculation incorporates imaging errors that are caused by the objective lens (aberrations), contrast aperture (diffraction), imperfect source characteristics, and voltage and current instabilities. It is used to evaluate the appearance of image features that arise from phase objects such as surface steps and amplitude objects that produce what is alternatively called amplitude, reflectivity or diffraction contrast in LEEM. This formalism can be used after appropriate modification to treat image formation in other emission microscopies. Implications for image formation in the latest aberration-corrected instruments are also discussed.

(Some figures in this article are in colour only in the electronic version)

1. Introduction

Image formation in cathode lens electron microscopy is primarily determined by the properties of the cathode objective lens, although optical components after the objective lens, such as beam separators and imaging electron filters, can modify to some extent the primary image formed by the cathode lens. Resolution and contrast are generally the two most important aspects in imaging, while image acquisition time can also be of importance in some imaging modes. In the past, most of the attention has been given to calculating resolution, usually using ray-optical methods. An exception is the early wave-optical calculation of the resolution in emission microscopy by Recknagel [1]. This approach produced results that differed significantly from those of his earlier ray-optical calculations. It is therefore desirable to perform wave-optical calculations also for energies beyond the range of validity of Recknagel's assumptions, for example for the energy range used in LEEM [2], and to calculate not only resolution but also contrast in a consistent manner for two limiting contrast mechanisms, pure phase contrast and pure amplitude contrast. Pure phase contrast is realized in atomic steps on a clean single-crystal surface. Pure amplitude contrast can occur on a flat surface at the sharp boundary between materials or structures with different reflection coefficients. Such a boundary is commonly found when two different structures coexist in the surface plane without an intervening step. It might also be realized by decoration of atomic surface steps with a material with different reflection coefficient consisting of atoms with the same diameter as the substrate atoms. The field distortions in front of such surfaces are minimal, which makes them ideal test objects of resolution and contrast. Until now, only a wave-optical model of step phase contrast in LEEM has been discussed [3, 4]. Although it reproduces the key image features that are observed experimentally, this model only treats the wave interference phenomenon at a step in an accurate way. It is not a complete calculation of image formation because the properties of the objective lens and diffraction at the contrast aperture were only included in a very ad hoc way. Therefore, we use Fourier optics in this paper, which can account for these effects rigorously.

2. Fourier optics of image formation

2.1. Elementary considerations

In the Fourier optics approach, the formation of the diffraction pattern and image in the microscope (figure 1) are synonymous with the Fourier transform of the wave that is emitted from the object and its subsequent inverse Fourier transform,

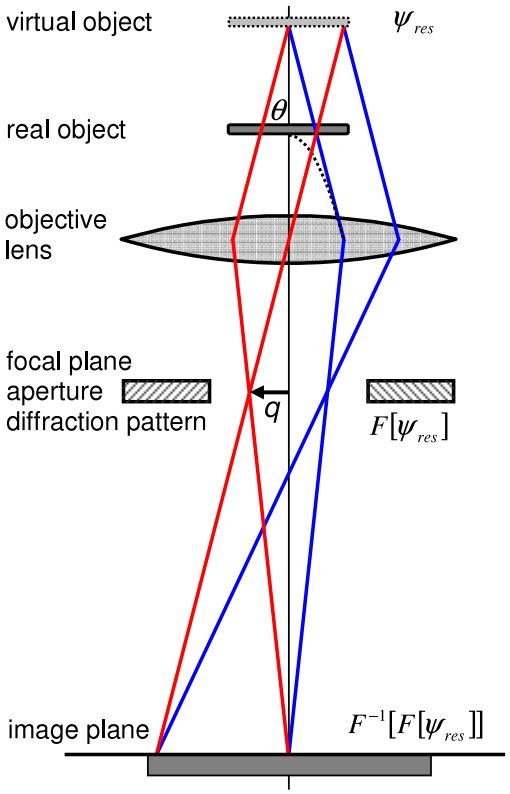

Figure 1. (Color online) Ray paths of emitted waves, ψ_{res}, that produce the diffraction pattern and image. The dashed line is the path of electrons that are accelerated in the objective lens to microscope potential. F and F^{-1} are the Fourier and inverse Fourier transforms, respectively.

respectively. Fourier optics treats the modifications of the ideal emitted wavefront that are caused by several factors, including source characteristics (source extension and energy spread) that define beam coherence, the action of the electron-optical elements (objective lens and contrast aperture) that produce a magnified image, as well as voltage and current instabilities. We outline below how the errors that are introduced by these factors are expressed in the transform and inverse transform [5]. This modeling follows the existing formalism that is used to describe image formation in transmission electron microscopy (TEM) [6–12]. However, one important characteristic of LEEM and other cathode lens microscopies that must be taken into account in this adaptation is that electrons that are reflected or emitted (commonly referred to as emitted in the following) from the sample, i.e. the real object, are accelerated from low emission energy, U_0, to the microscope potential, U, in the objective lens. This creates a virtual object plane behind the real object plane (figure 1) at a distance, a, from the objective lens that is of the order of the focal length, f, $a \gtrsim f$. The virtual plane is absent in TEM because such acceleration does not take place. Therefore, the formulation of the Fourier optics calculation here refers to the virtual rather than the real object in LEEM. The relation between the virtual and real objects and the recovery of real object information are discussed further in the appendix.

We begin by considering the illumination of a sample by a uniform plane wave at normal incidence, $\psi_{\text{ill}}(\bar{r}) = \psi_0 \exp(\mathrm{i}\bar{k}\cdot\bar{r}) = \psi_0 \exp(\mathrm{i}kz)$, where z is the position along the optical axis of the illumination, ψ_0 is the amplitude and $k = 2\pi/\lambda$ is the momentum wavevector. The wavelength of the incident wave at the virtual object, λ, is equal to the wavelength after acceleration from the real object. Upon interaction with the sample, the incident wave is modified by a position-dependent object function. In a one-dimensional model of the object, the object function has the form $\psi_{\text{obj}}(x) = \sigma(x)\exp(\mathrm{i}\phi(x))$, where x is the lateral position in the virtual object plane, and σ and ϕ are the amplitude and phase, respectively. Features that cause a spatial variation of the amplitude give rise to what is alternatively called amplitude, reflectivity or diffraction contrast in LEEM. Features that cause a spatial variation of the phase, such as surface steps in LEEM, produce phase contrast.

The emitted wave is given by $\psi_{\text{res}}(\bar{r}) = \psi_{\text{ill}}(\bar{r})\cdot\psi_{\text{obj}}(x)$. For a uniform illumination, the emitted wavefront in the virtual object plane is equal to the object function multiplied by the illumination, $\psi_0\exp(\mathrm{i}kz)$. For convenience, we set $\psi_0 = 1$ and $z = 0$ at the virtual object plane so that $\psi_{\text{ill}}(z=0) = 1$. The influence of the illumination will be taken into account later in section 2.3. The emitted wave can be expressed as a sum of plane waves, $\exp(\mathrm{i}\bar{k}_f\cdot\bar{r})$, where $k_f = k$, which are emitted from the virtual object at various angles θ with respect to the optical axis (figure 1). The use of the set of plane waves that are emitted from the virtual object to describe the wavefront in the virtual object plane restricts the position vector to the virtual object plane, $\bar{r} = \bar{x}$. Therefore, the plane waves can be rewritten as $\exp(\mathrm{i}\frac{2\pi}{\lambda}x\sin\theta) = \exp(\mathrm{i}2\pi qx)$, where the spatial frequency is approximated as $q = \theta/\lambda$ for paraxial rays. The paraxial ray approximation should be generally valid for emission from the virtual object in cathode lens microscopy using low energy electrons ($U_0 \ll U$). Equating the wavefront in the virtual object plane with the object function, the plane wave sum is written as

$$\psi_{\text{res}}(x) = \psi_{\text{obj}}(x) = \int \tilde{\psi}_{\text{obj}}(q)\exp(\mathrm{i}\,2\pi qx)\,\mathrm{d}q,$$

with amplitudes that are given by the Fourier transform of the object function:

$$\tilde{\psi}_{\text{res}}(q) = \tilde{\psi}_{\text{obj}}(q) = F[\psi_{\text{obj}}(x)] = \int \psi_{\text{obj}}(x)\exp(-\mathrm{i}\,2\pi qx)\,\mathrm{d}x. \quad (1)$$

Each plane wave is focused to a different point in the back focal plane of the objective (figure 1). Therefore, the amplitudes expressed by equation (1) also represent the diffraction pattern that appears in the back focal plane. The wave that forms the image in the image plane (figure 1) is given by the inverse Fourier transform:

$$\psi_m(x) = F_{M_0}^{-1}[\tilde{\psi}_{\text{res}}(q)] = \frac{1}{M_0}\int \tilde{\psi}_{\text{res}}(q)\exp\left(\mathrm{i}2\pi q\frac{x}{M_0}\right)\mathrm{d}q, \quad (2)$$

where the factor $1/M_0$ takes into account the reduction of the amplitude ψ_{res} and the change of length scale by the magnification M_0. Being a constant, we will take the magnification to be 1 in the following for convenience. In sections 2.2 and 2.3, we outline how numerous factors modify

the ideal transforms expressed by equations (1) and (2). The image intensity that is formulated using a modified form of equation (2) is presented in section 2.4.

2.2. Diffraction error and wave aberrations

A contrast aperture in the back focal plane limits the range of the emission angle that is used for image formation (figure 1). The aperture produces diffraction that degrades resolution [6–8]. This effect is modeled in Fourier optics by including a multiplicative factor inside the integral expression for the image wave, equation (2), of the form

$$M(q) = \begin{cases} 1 & \text{for } |q| < q_{\max} \\ 0 & \text{for } |q| \geqslant q_{\max}, \end{cases} \tag{3}$$

where $q_{\max} = \alpha_{\text{ap}}/\lambda$ and α_{ap} is the maximum emission angle permitted by the aperture. This angle is determined by the radius of the aperture, r_{ap}, and the distance of the virtual object from the objective lens, $\sim r_{\text{ap}}/a$. If the aperture is physically positioned in a subsequent diffraction plane in the microscope, then the appropriate magnification factor between the two diffraction planes should be considered.

Wave aberrations refer to deviations of the wave path from ideal (figure 2(a)). These deviations come from two sources: focusing errors of wavefronts that follow trajectories off the optical axis, referred to as spherical aberrations, and deviations of the focal length or sample position from ideal values, together referred to as defocus. These two errors are considered together because they both produce optical path length differences for off-axis waves ($q > 0$) compared to the on-axis wave. This is equivalent to a q-dependent phase shift that is given by [5–9]

$$W(q, \Delta z) = \tfrac{1}{4}\left(C_{\text{S}}\lambda^3 q^4 - 2\Delta z \lambda q^2\right), \tag{4}$$

where C_{S} is the spherical aberration coefficient of the objective lens and $\Delta z = \Delta f - \Delta a$ is the defocus with Δf and Δa being the deviations of focus and sample position, respectively, from ideal values (figure 2(a)).

Together, the diffraction error and wave aberrations introduce a multiplicative factor in the inverse transform, equation (2), that is given by

$$H(q, \Delta z) = M(q)\exp(\text{i}2\pi\, W(q, \Delta z)).$$

2.3. Beam coherence and stability

In a real instrument, instabilities of lens current and voltage and imperfect source characteristics that diminish beam coherence will introduce errors in image formation. We consider the effect of two factors that define beam coherence, source extension and energy spread. First of all, electrons are emitted from a confined area on a cathode rather than from a point source. Consequently, an electron that is emitted from a position some distance away from the point on the optical axis will be incident with a tilt angle, call it τ, at the sample. In the Fourier analysis, the q-mode component of the emitted

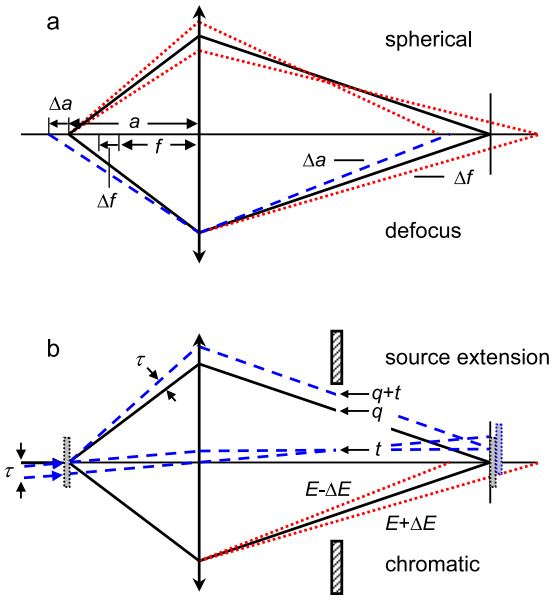

Figure 2. (Color online) Deviations in ray path (solid lines) that are caused by (a) spherical aberration (upper dashed lines) and defocus (lower dashed lines) and (b) source extension (upper dashed lines) and chromatic aberration (lower dashed lines) are shown. The defocus error is caused by displacement of the object position, a, and adjustment of the focal length, f, from ideal. The convention for positive changes of these variables, Δa and Δf, is shown. The other variables are defined in the text.

wave from this off-axis point source will be shifted by a corresponding amount, $t = \tau/\lambda$, from q to $q + t$ compared to the same mode that is produced by the on-axis point source (figure 2(b)). The extended source can be described by a source density with a Gaussian distribution [10, 11]

$$s(t) = \frac{1}{\sqrt{\pi}\, q_{\text{ill}}} \exp\left[-\left(\frac{t}{q_{\text{ill}}}\right)^2\right],$$

where $q_{\text{ill}} = \alpha_{\text{ill}}/\lambda$ and α_{ill} is related to the full width at half-maximum of the angle subtended by the extended source density when viewed from the on-axis point on the virtual object. The final image will be calculated in section 2.4 by summing the contributions from all points on the cathode weighted by the source density.

The energy spread of the electron beam also produces errors during image formation because of chromatic aberration of the lens. This refers to deviations of electron trajectories from the nominal trajectory that are produced by the energy dependence of the focal length (figure 2(b)). Chromatic aberrations are included in the calculation by summing the weighted contributions for the different energies within the (assumed) Gaussian energy distribution of the source. The Gaussian weighting function, called the defocus distribution, has a width $\Delta f_{CE} = C_{CE}(\Delta E/E)$, where C_{CE} is the chromatic aberration coefficient and ΔE is the width of the energy distribution about the nominal energy E [11]. Instabilities in the lens voltage and current also produce fluctuations of the lens focal length. If these instabilities are time-averaged, they have an effect on image formation that is

analogous to that which is produced by energy spread [12]. Instabilities are therefore described by their respective defocus distributions, assumed to be Gaussian. Energy spread and instabilities are combined by convolution in the composite defocus distribution [7, 8, 11]

$$c(\Delta z_c) = \frac{1}{\sqrt{\pi}\Delta f_C} \exp\left[-\left(\frac{\Delta z_c}{\Delta f_C}\right)^2\right], \quad (5)$$

where Δz_c is the defocus integration variable used in the calculation of image intensity and Δf_C is the width of the convolved defocus distribution. The width is given by

$$\Delta f_C^2 = C_{CE}^2\left(\frac{\Delta E}{E}\right)^2 + C_{CU}^2\left(\frac{\Delta U}{U}\right)^2 + C_{CI}^2\left(\frac{\Delta I}{I}\right)^2, \quad (6)$$

where C_{CU} and C_{CI} are the respective chromatic aberration coefficients for voltage and current instabilities, ΔU and ΔI are the widths of the time-averaged voltage and current distributions about the nominal voltage and current, U and I, respectively, and $E = U$ for the virtual object here.

2.4. Image formation

The image intensity is calculated as the product of the wavefunction and its complex conjugate, $I(x) = \psi_m(x) \cdot \psi_m^*(x)$. The modifications of the inverse transform, equation (2), due to the several factors that are described in sections 2.2 and 2.3, are collected in a reflection cross-coefficient, $R(q, q', \Delta z)$, in the expression for the intensity [6]

$$I(x) = \int_q \int_{q'} \tilde{\psi}_{res}(q) \cdot \tilde{\psi}_{res}^*(q')\, R(q, q', \Delta z) \times \exp(i\,2\pi(q - q')x)\, dq\, dq'.$$

Considering first only wave aberrations and diffraction error, the reduced cross-coefficient is given by

$$R_0(q, q', \Delta z) = H(q, \Delta z)\, H^*(q', \Delta z) = M(q)M^*(q') \times \exp[i2\pi(W(q, \Delta z) - W(q', \Delta z))]. \quad (7)$$

The reduced cross-coefficient must be integrated over the source density and defocus distributions to obtain the complete cross-coefficient that includes the effects of beam coherence and instabilities:

$$R(q, q', \Delta z) = \int\int s(t)c(\Delta z_c)R_0(q + t, q' + t, \Delta z + \Delta z_c) \times dt\, d\Delta z_c.$$

It is useful to simplify the cross-coefficient by expanding the phase shift $W(q + t, \Delta z + \Delta z_c)$ in a Taylor series, keeping only up to the first-order terms in the small quantities Δz_c and t [10, 11]. Assuming $t \ll q, q'$ and approximating $M(q + t) \approx M(q)$, we obtain the following expression:

$$R(q, q', \Delta z) = R_0(q, q', \Delta z)\, E_s(q, q', \Delta z)\, E_c(q, q'), \quad (8)$$

where

$$E_s(q, q', \Delta z) = \exp[-\pi^2 q_{ill}^2(C_S\lambda^3(q^3 - q'^3) - \Delta z\lambda(q - q'))^2], \quad (9)$$

and

$$E_c(q, q') = \exp[-\pi^2 \Delta f_C^2 \lambda^2 (q^2 - q'^2)^2]. \quad (10)$$

The physical meaning of the three factors that make up R can be understood as follows. First, R_0 contains $M(q)$ and $\exp(i2\pi W(q))$, which are clearly the effects of diffraction at the contrast aperture and wave aberrations, respectively. The factor E_s contains the product of the source extension parameter, q_{ill}, and the partial derivative $\partial W/\partial q$. This means that source extension comes into play only through wave aberrations of the objective lens. If the spherical aberration coefficient and defocus are both zero, then source extension has no effect. Therefore, we attribute E_s to the effect of source extension. It is also evident that the factor E_c is due to chromatic aberrations associated with energy spread and instabilities.

3. Results and discussion

We calculate image features here that are produced by pure phase and pure amplitude objects. The spatial variations of phase and amplitude that are caused by these objects are represented by the abrupt step functions in the respective variables that are shown in figure 3. A surface step is an example of a pure phase object that causes a phase shift but has no effect on the amplitude. The phase shift is given by $\phi = kd = (2\pi/\lambda_0)2a_0$, where $d = 2a_0$ is the path length difference between waves that are reflected from terraces on opposite sides of a step, a_0 is the step height and λ_0 is the wavelength of low energy electrons that are elastically backscattered from the surface, i.e. the real object. For the reflection geometry of LEEM, the positive phase shift at positive coordinates in figure 3 represents the additional path length that a wave travels to and from the terrace on the lower side of the step. Conversely, a pure amplitude object produces a change of the amplitude, but has no effect on the phase. Such a situation may arise when two structures are present that produce different diffraction intensities. We consider the extreme case that the contrast of the object amplitude function is 100%. The behavior of weaker amplitude objects is related trivially to the case that is calculated. The behavior of mixed phase/amplitude objects can also be calculated by the same methods.

3.1. Effect of cross-coefficient

In order to illustrate the influence of the various factors that are included in the cross-coefficient, we plot the quantities related to wave aberrations, $\exp[i2\pi(W(q, \Delta z) - W(0, \Delta z))]$, source extension, $E_s(q, 0, \Delta z)$, and chromatic aberration, $E_c(q, 0)$, in figure 4. These quantities are shown for in-focus and out-of-focus conditions, where appropriate. Defocus is specified in units of the reduced defocus, $\Delta z^* = \Delta z(C_S\lambda)^{-1/2}$, which is defined in the appendix. The effects of these factors on image formation are demonstrated in the calculated image intensity profiles that are shown for in-focus and out-of-focus conditions in figure 5. Lateral position in figure 5 is specified in terms of the real object coordinate, x_0. The parameters that are used in the calculation and the relationships between the real

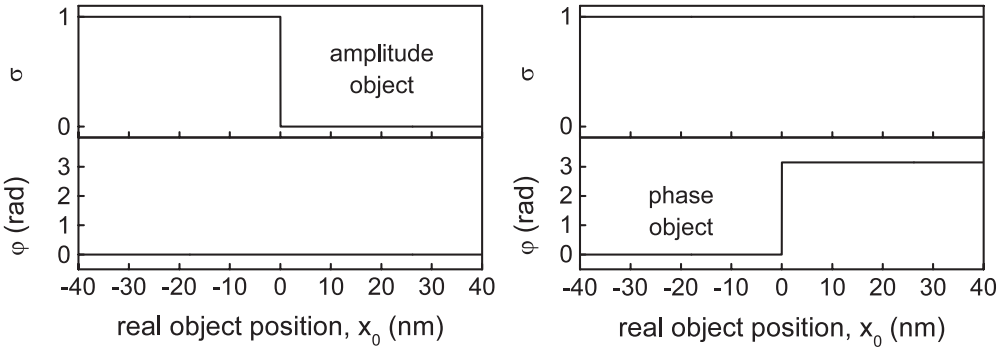

Figure 3. The amplitude, σ, and phase, ϕ, components of the object function are shown for amplitude and π-phase objects.

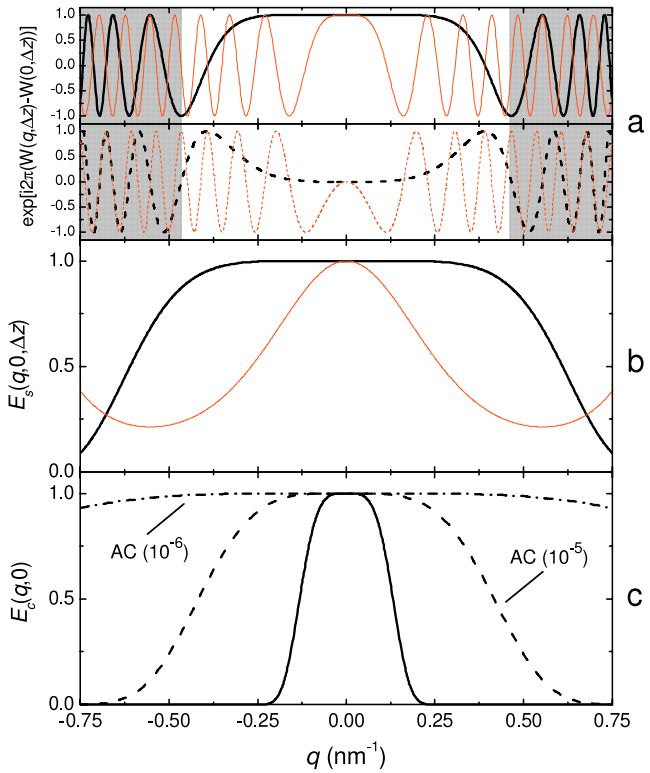

Figure 4. (Color online) Factors that comprise the complete reflection cross-coefficient (equation (8)) are plotted for in-focus ($\Delta z^* = 0$, thick lines) and out-of-focus ($\Delta z^* = 6$, thin red lines) conditions. In (a), the real (solid lines) and imaginary (dashed lines) parts of the wave aberration function are shown. The gray shaded region is blocked by the aperture function, $M(q)$. The source extension function is shown in (b). In (c), the chromatic aberration function is shown for $\Delta E = 0.5$ eV and the aberration coefficients C_{CE}, C_{CU} and C_{CI} stated in the appendix (solid line) and for aberration correction (AC) with $C_{CE} = 0$ and instability levels $\Delta I/I = \Delta U/U = 10^{-5}$ (dashed line) and 10^{-6} (dotted–dashed line).

and virtual coordinates and parameters are discussed in the appendix.

The aperture function, $M(q)$, suppresses modes in the Fourier transform above a sharp cutoff. For the virtual aperture angle used in the calculation, $\alpha_{ap} = 4.15$ mrad (see the appendix), the cutoff is at $q_{max} = 0.458$ nm^{-1} (see figure 4(a)). We know from textbook descriptions that the complete reproduction of sharp features such as the amplitude object step function in figure 3 by Fourier series requires an infinite number of q-mode terms. The loss of high q modes caused by the use of an aperture introduces broadening and intensity fringes (figure 5(a)), with respective width and spacing that scale with the inverse of the cutoff q_{max}. This is the well-known diffraction effect that produces the diffraction limit in resolution [6–8]. The effect for the phase object is more profound (figure 5(e)). Namely, the aperture produces phase contrast in the calculation. For the π-phase object, diffraction fringes are arranged symmetrically about a core destructive fringe that is located at the position of the phase jump in the phase object step function (figure 3). Just as for the amplitude object, the fringe spacing and core width scale with the inverse of q_{max}. In the limit that α_{ap} and q_{max} go to infinity, the lateral dimensions of the phase object features approach zero in the image and phase contrast is lost. The same fundamental effect is caused by the other factors that act as low pass filters and suppress the high q modes in the calculation.

The real part of the wave aberration function (figure 4(a)) is equal to one for small values of q at the in-focus condition, $\Delta z^* = 0$, but it oscillates rapidly at large values of q. This oscillation produces additional intensity fringes that are detrimental to image formation. The imaginary part exhibits similar oscillations at large q, but is not important at small q for the in-focus condition because it is zero. By making a proper choice of the aperture that cuts off the wave aberration function oscillations at large q, their influence can be avoided. This is the case for the aperture cutoff and in-focus wave aberration function that are indicated in figure 4(a). Consequently, the appearance of image features that are produced by aperture diffraction error only (figures 5(a) and (e)) are modified only slightly by wave aberrations at the in-focus condition (figures 5(b) and (f)). On the other hand, defocus shifts the onset of the aberration function oscillations to smaller q and, at the same time, effectively narrows the range at small q over which the real part of the aberration function is unity (figure 4(a)). This produces broader amplitude and phase object features and increases fringe spacing in the image (figures 5(b) and (f)), qualitatively similar to the effect of reducing q_{max}.

The source extension function also suppresses large q modes at the in-focus condition (figure 4(b)). For the set of parameters used in our calculation, the small q modes that are

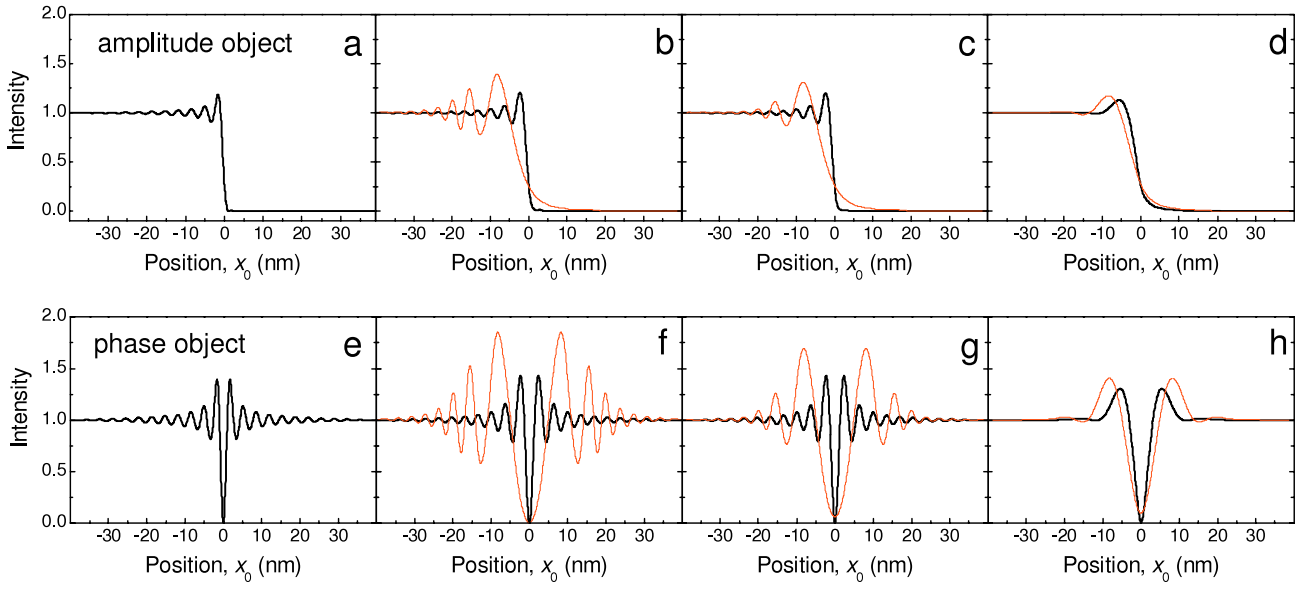

Figure 5. (Color online) Calculated images of amplitude and π-phase objects (figure 3) are shown that are obtained using (a), (e) aperture function $M(q)$ only, (b), (f) aperture and wave aberration function (equation (7) and figure 4(a)), (c), (g) aperture, wave aberrations and source extension function, E_s (equation (9) and figure 4(b)), (d), (h) aperture, wave aberrations, source extension and chromatic aberration function, E_c (equation (10) and figure 4(c)). The intensity profiles are shown for in-focus ($\Delta z^* = 0$, thick lines) and out-of-focus ($\Delta z^* = 6$, thin red lines) conditions. The abscissa is the real object position.

passed without modification by the source extension function fall in a range of q that is broader than the range of the aperture and wave aberration function in-focus. Therefore, the appearance of image features is unaltered when source extension is included for the in-focus condition (figures 5(c) and (g)). This will also be true for out-of-focus conditions up to a point. That point is reached when the narrowing effect of defocus on the source extension function begins to exceed its narrowing of the wave aberration function. That point has been passed for the defocus value that was used to produce the defocus curves in figures 4(a) and (b). In this case, fringe amplitudes are decreased and fringe spacing is increased slightly in the out-of-focus condition when the effect of source extension is included (figures 5(c) and (g)).

The chromatic aberration function also suppresses large q modes, but the range of unmodified modes at small q is the narrowest among the factors considered here for the in-focus condition (figure 4(c)). This leads to the suppression of all but the strongest fringes in the image. Chromatic aberrations also have the dominant effect on the feature width at the in-focus condition (figures 5(d) and (h)). This observation is consistent with our understanding of the importance of chromatic aberrations in defining cathode lens microscope resolution [13]. The effect of chromatic aberrations on image features is independent of the focus condition. Therefore, wave aberrations and source extension exert a greater influence with increasing defocus (figures 5(d) and (h)) and can eventually overtake chromatic aberrations in determining feature size and resolution.

3.2. Step phase contrast

Atomic steps are a very common defect at surfaces that have been imaged very nicely using LEEM on many surfaces. The step phase contrast mechanism has already been explored using a wave-optical model [3, 4]. This revealed that a rich interference phenomenon occurs at a step. The detrimental effects of imperfect source characteristics on the 'imaging' wave were included as rigorously as possible in the limited context of the wave-optical model. However, aberrations were treated only in an ad hoc way by Gaussian convolution of the wave amplitude, and diffraction error was not included at all. It would therefore be interesting to make a comparison between the results of the Fourier optics calculation, which treats these influences more realistically, and the earlier wave-optical model calculations of step phase contrast.

Figure 6 shows the phase shift and focus dependence of phase contrast that are determined by the Fourier optics calculation using the complete cross-coefficient (equation (8)). These figures reproduce the key results of the wave-optical model calculation of step contrast. In the out-of-phase condition, $\phi = (2n + 1)\pi$ where $n =$ integer, the Fourier optics calculation produces equivalent intensity maxima that are located symmetrically about a complete destructive interference fringe at the step position. In the in-phase condition, $\phi = 2n\pi$, contrast is absent. Clearly asymmetric features are observed at the intermediate phase conditions that are most pronounced at $\phi = (2n + 1)\pi/2$. We identify the positive coordinate in figures 3 and 6 with the terrace on the lower or down-side of a step. For $\phi = \pi/2$ and equivalent intermediate phase conditions ($n =$ even), an intensity maximum (minimum) is located on the down- (up-) side of the step for positive defocus. For $\phi = 3\pi/2$ and equivalent conditions ($n =$ odd), the asymmetry is reversed with an intensity maximum (minimum) located on the up- (down-) side of the step for positive defocus. The locations of the maxima and minima also flip to the opposite sides of the step for

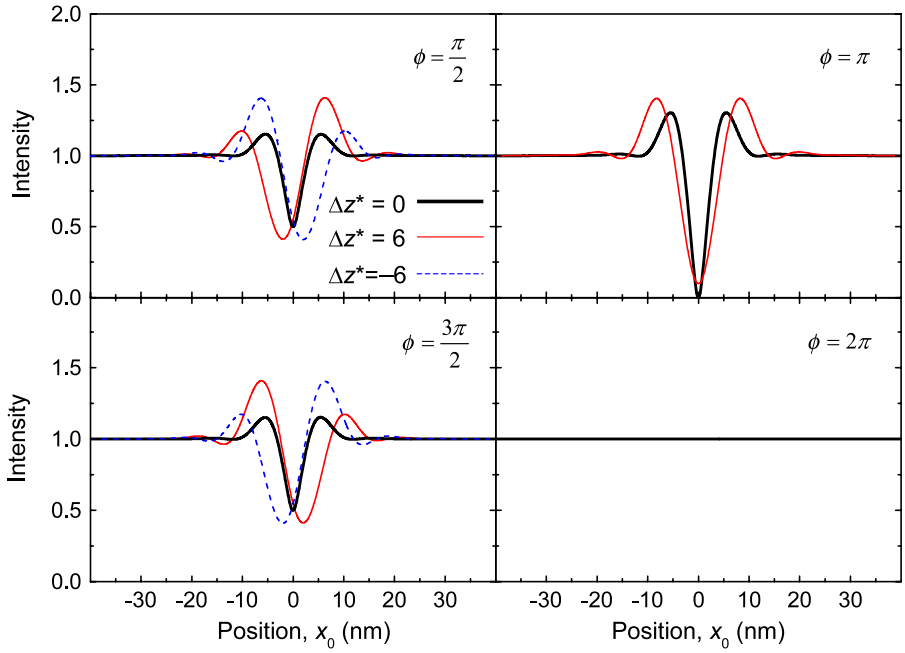

Figure 6. (Color online) The phase shift dependence of phase contrast is shown for in-focus ($\Delta z^* = 0$, thick solid lines), underfocus ($\Delta z^* = 6$, thin solid red lines) and overfocus ($\Delta z^* = -6$, thin dashed blue lines) conditions. For $\phi = \pi$, positive and negative defocus produce identical intensity profiles. For $\phi = 2\pi$, the absence of contrast features is independent of focus condition. The abscissa is the real object position.

these two intermediate phase conditions at negative defocus. For the π out-of-phase condition, the symmetric features are identical for positive and negative defocus and broadened compared to in-focus. Such defocus broadening is generally true for all phase conditions and is consistent with experimental observations and the wave-optical model predictions [3, 4]. For the 2π in-phase condition, however, the absence of contrast is independent of the focus condition. According to our convention, $\Delta z = \Delta f - \Delta a$ for Δf and Δa shown in figure 2(a), positive (negative) defocus corresponds to an increase (decrease) of the focal length for $\Delta a = 0$. This is achieved in the magnetic objective lens by decreasing (increasing) the excitation of the objective lens current from the value for the in-focus condition. Consequently, positive and negative defocus are called under- and overfocus, respectively. As pointed out earlier [3, 4], an understanding of asymmetric step phase contrast features, coupled with knowledge of the phase shift and defocus condition, can be put to practical use to identify the step sense simply by visual inspection of the images.

The Fourier optics calculation also reveals something interesting that was not discussed before. In particular, it indicates the presence of symmetric contrast features in-focus for all phase conditions, excluding the $\phi = 2n\pi$ in-phase conditions, that resemble the $\phi = (2n + 1)\pi$ out-of-phase form. The depth of the destructive intensity minima at the core and the height of the bordering fringes decrease towards zero as the phase is changed from the $(2n + 1)\pi$ out-of-phase to the $2n\pi$ in-phase condition. This result is somewhat surprising because it contradicts the common experimental observation that step contrast vanishes at the in-focus condition for all phase shifts. The cause of this discrepancy is not understood. In terms of the Fourier optics formalism presented here, there is nothing that can be adjusted that can suppress phase contrast at the in-focus condition. Although the instability level used in the calculation produces negligible effect on image features (see section 3.3), greater instabilities should act in a way that is very similar to energy spread because they both come into the calculation through the chromatic aberration function. Therefore, instabilities are unlikely to be responsible for extinguishing in-focus step contrast. The source of the discrepancy may lie elsewhere on the experimental side.

3.3. Resolution, aberration correction and further applications

The instrument resolution that is defined by the width of the amplitude object edge in focus is shown in figure 7. The 84%/16% criterion that is used to determine the resolution is shown in the inset of this figure. The improvement of resolution with increasing energy that is predicted by the Fourier optics calculation is consistent with behavior that was predicted already in the early years of LEEM [13]. The distance between the intensity maxima and the central minimum that appear in the image of a π-phase object in focus at 10 eV (figure 5(h)) is shown in figure 7 for comparison. The phase object feature distance is approximately equivalent to the resolution that would be determined from the amplitude object using a less favorable 90%/10% criterion.

We find that the effect of instabilities of $\Delta I/I = \Delta U/U = 10^{-5}$ on image formation is negligible compared to chromatic and spherical aberrations for the typical instrumental energy spread $\Delta E = 0.5$ eV and aberration coefficients used here. However, in instruments that correct these aberrations,

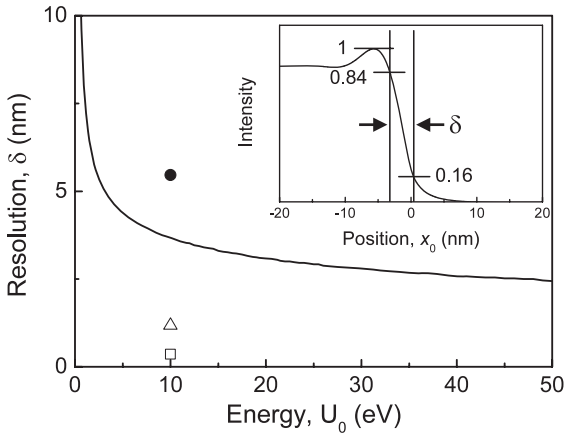

Figure 7. Instrumental resolution determined from the in-focus amplitude object image profile using the 84%/16% condition (inset) is shown with aberrations for $\Delta E = 0.5$ eV (solid line) and without aberrations ($C_{CE} = C_S = 0$) for instability levels of $\Delta I/I = \Delta U/U = 10^{-5}$ (△) and 10^{-6} (□). The separation of π-phase object first-order maxima and central minimum in focus and with aberrations is also shown (●). This corresponds to the Raleigh criterion.

such that C_S and C_{CE} may be taken to be zero, it is possible that instabilities are more important. The reduction of instabilities by up to an order of magnitude is not only possible but may even be necessary to achieve optimal resolution in aberration-corrected instruments. Let us examine the effect of C_S and C_{CE} correction on the Fourier optics calculation. Since wave aberrations are absent in the calculation for this correction in focus (C_S and Δz are zero in R_0), angular confinement by the aperture is no longer necessary. Source extension is also unimportant (since C_S and Δz are zero in E_s). The chromatic aberration function, E_c, also only has an effect on image formation through instabilities ($C_{CE} = 0$, $C_{CU} \neq 0$, $C_{CI} \neq 0$) and is correspondingly broader than without aberration correction. This is shown in figure 4(c) for instability levels of 10^{-5} and 10^{-6}. Therefore, the calculation for aberration correction is carried out with an aperture that does not cut off the E_c function, or with no aperture at all. The resolution that is determined from the amplitude object image with aberration correction is indicated in figure 7. This demonstrates that the improvement of resolution that can be achieved with aberration correction and by reducing instabilities *within the context of the Fourier optics calculation presented here* is significant. It should be noted, however, that the calculation considers the chromatic and spherical aberrations of lowest order only. Therefore, the resolution for aberration correction is determined only by instabilities here. Not surprisingly, it is better than what is determined for aberration-corrected instruments when higher-order aberrations that are not corrected are taken into account [14]. Nevertheless, attention to voltage and current instabilities may still bring some practical benefit for achieving the optimal resolution of aberration-corrected instruments.

Although Fourier optics has been discussed in the context of LEEM, the formalism presented here can also be adapted for describing image formation in another popular cathode lens microscopy, photoemission electron microscopy (PEEM). In PEEM, images are formed using photoelectrons that are produced by illumination of the sample with light. The different excitation source in PEEM eliminates the need to consider source extension in the model calculation. In LEEM, the emission of elastically backscattered electrons is concentrated at the Bragg angles by diffraction. Selection of a single diffraction spot on the optical axis with the contrast aperture provides a sufficiently high signal for fast imaging with low noise. In PEEM, however, photoelectrons are emitted from the real object more uniformly over a broad range of angles than in LEEM. Nevertheless, the emission angles from the virtual object are sufficiently small in the UV and near-XUV range so that the paraxial ray approximation remains valid. From the viewpoint of improving transmission and signal intensity in PEEM, it is common practice to use a larger aperture angle. In the calculation, this is accomplished by using an aperture function $M(q)$ (equation (3)) that passes a larger range of spatial frequencies. Although this reduces or eliminates the diffraction error, it enhances the effect of wave aberrations (equations (4) and (7)). The use of a larger energy window, ΔE, to increase transmission also has the drawback of enhancing chromatic aberrations through the function E_c (equation (10)). Higher-order spherical and chromatic aberrations that were not considered here also become important under these conditions of higher transmission [14].

4. Conclusion

Fourier optics allows us to describe image formation in cathode lens electron microscopy in a comprehensive manner by taking into account the lowest order spherical and chromatic aberrations of the objective lens, diffraction at the aperture, energy spread and size of the electron source in LEEM as well as instabilities of the lens current and the high voltage. This has been illustrated for two limiting contrast mechanisms in LEEM, pure phase contrast and pure amplitude contrast. The calculations clearly show the influence of the various factors that determine the intensity distribution in the image and the dominating effect of the chromatic aberration that was predicted already in the early years of LEEM. Aberration correction improves the resolution to 1 nm but a resolution of 1 Å will require not only correction of higher-order aberrations but also extreme electrical and mechanical stability. With amplitude contrast a resolution of a few nm should be achievable, using a field emission electron source, already without aberration correction, in particular at higher energies.

Appendix. Parameters for LEEM

Section 2 describes the formation of an image of the virtual object. We describe here how the virtual object parameters and coordinates referred to in section 2 are related to those of the real object in LEEM. The values of the parameters that are used to produce the results in section 3 are also presented in this appendix. First, we define the immersion factor $\kappa = U/U_0$, where U_0 is the emitted electron energy at the sample before acceleration and U is the kinetic energy after acceleration to the microscope potential. The ratio of the wavelengths at the

real and virtual object planes, λ_0 and λ, respectively, is given accordingly by $\lambda/\lambda_0 = \kappa^{-1/2}$. The relationships between the real (x_0, θ_0) and virtual (x, θ) spatial and angular coordinates are $x/x_0 = M_\mathrm{L}$ and $\theta/\theta_0 = M_\mathrm{A}$, respectively, where M_L is the lateral magnification and M_A is the angular magnification. Because of the inverse relationship between spatial coordinate, x, and spatial frequency, q, expressed as $q = \theta/\lambda \sim 1/x$, the spatial frequencies associated with the virtual, q, and real, q_0, objects are related according to $q = q_0/M_\mathrm{L}$. Furthermore, it is straightforward to show that M_L and M_A are related by

$$M_\mathrm{A} = (\kappa^{1/2} M_\mathrm{L})^{-1}. \tag{A.1}$$

The virtual aperture and illumination angles are also expressed in terms of the corresponding real object angles as $\alpha_\mathrm{ap} = \alpha_{\mathrm{ap}0} M_\mathrm{A}$ and $\alpha_\mathrm{ill} = \alpha_{\mathrm{ill}0} M_\mathrm{A}$, respectively.

In order to find the relationship between real and virtual spherical aberration coefficients, it is helpful to change variables in the expression for the phase shift due to wave aberrations (equations (4))

$$W(\theta^*, \Delta z^*) = \frac{\theta^{*4}}{4} - \frac{\theta^{*2}}{2}\Delta z^*,$$

where $\theta^* = q\lambda(C_\mathrm{S}/\lambda)^{1/4}$ and $\Delta z^* = \Delta z (C_\mathrm{S}\lambda)^{-1/2}$. Since image features and contrast should have the same appearance regardless of whether we perform the calculations using real or virtual coordinates/parameters, the quantities θ^* and Δz^* must be invariant under such a coordinate transformation. Thus, we can write the equalities $\theta^* = \theta_0^*$ and $\Delta z^* = \Delta z_0^*$, where the '0'-subscripted variables, $\theta_0^* = q_0\lambda_0(C_{\mathrm{S}0}/\lambda_0)^{1/4}$ and $\Delta z_0^* = \Delta z_0 (C_{\mathrm{S}0}\lambda_0)^{-1/2}$, and the parameters contained within are associated with the real object. From these equalities, we derive the desired relationships:

$$\frac{\Delta z}{\Delta z_0} = \kappa^{1/2} M_\mathrm{L}^2, \tag{A.2a}$$

$$\frac{C_\mathrm{S}}{C_{\mathrm{S}0}} = \kappa^{3/2} M_\mathrm{L}^4. \tag{A.2b}$$

The relationships between the real and virtual chromatic aberration coefficients are found by applying a similar coordinate transformation to the widths of the Gaussian defocus distributions (of the form of equations (5)) that are produced individually by energy spread ($\Delta f_{CE} = C_{CE}\ (\Delta E/E)$), voltage ($\Delta f_{CU} = C_{CU}\ (\Delta U/U)$) and current ($\Delta f_{CI} = C_{CI}\ (\Delta I/I)$) instabilities, and by noting that the defocus distribution must be invariant under these transformations. This means that the equalities $\Delta z_\mathrm{c}/\Delta f_{CE} = \Delta z_{\mathrm{c}0}/\Delta f_{CE0}$, $\Delta z_\mathrm{c}/\Delta f_{CU} = \Delta z_{\mathrm{c}0}/\Delta f_{CU0}$, and $\Delta z_\mathrm{c}/\Delta f_{CI} = \Delta z_{\mathrm{c}0}/\Delta f_{CI0}$ must hold, where the '0' subscripts again refer to the real object. From these equalities and equation (A.2), we obtain the relationships

$$\frac{C_{CE}}{C_{CE0}} = \frac{C_{CU}}{C_{CU0}} = \frac{C_{CI}}{C_{CI0}} = \kappa^{3/2} M_\mathrm{L}^2. \tag{A.3}$$

Note that, in order to derive equation (A.3), we have used $E = U_0$ in $\Delta f_{CE0} = C_{CE0}\ (\Delta E/E)$ for the real object and $E = U$ in $\Delta f_{CE} = C_{CE}\ (\Delta E/E)$ for the virtual object, while ΔE is the same for both and taken to be 0.5 eV in the evaluation described in section 3. Instabilities of $\Delta U/U = \Delta I/I = 10^{-5}$ are also assumed for the calculation.

Table A.1. Real object parameters calculated in [15] for $U = 18$ kV and $U_0 = 10$ eV and the virtual parameters for the magnetic objective lens.

Real object parameters		Virtual object parameters	
$\alpha_{\mathrm{ap}0}$	1.15×10^{-1} rad	α_ap	4.15×10^{-3} rad
$\alpha_{\mathrm{ill}0}$	6.93×10^{-3} rad	α_ill	0.25×10^{-3} rad
$C_{\mathrm{S}0}$	4.03×10^{-6} m	C_S	55.8×10^{-3} m
C_{CE0}	1.84×10^{-6} m	C_{CE}	59.8×10^{-3} m
C_{CU0}	2.25×10^{-7} m	C_{CU}	7.33×10^{-3} m
C_{CI0}	4.60×10^{-7} m	C_{CI}	15.0×10^{-3} m
U_0	10 eV	U	18 keV
λ_0	3.878 Å	λ	9.141×10^{-2} Å

The real object parameters, from which we derive the virtual object parameters by the preceding relations, have been calculated by Adamec for a magnetic objective lens that is similar to those that are currently in wide use [15]. For $U_0 = 10$ eV ($\lambda_0 = 3.878$ Å) and $U = 18$ keV ($\lambda = 9.141 \times 10^{-2}$ Å), the magnification factors were calculated to be $M_\mathrm{L} = 0.653$ and $M_\mathrm{A} = 3.61 \times 10^{-2}$ [15]. For the same values of U and U_0, the real object parameters shown in table A.1 were determined. These parameters were used to derive the virtual object parameters, also listed in table A.1, by the preceding relations.

In order to model image formation at other emission energies, U_0, we must understand how the key parameters depend upon energy. The total image magnification is a product of M_L and the magnification that is produced by the electron optics, M_0 (see equation (2)). The very weak dependence of total image magnification upon emission energy which is observed experimentally demonstrates the near-invariance of M_L. Therefore, we take the lateral magnification factor to be constant and equal to the value calculated by Adamec [15]. It follows that the energy dependence of the aperture, α_ap, and illumination, α_ill, angles is given only by the explicit κ dependence in equation (A.1). The energy dependence of the virtual aberration coefficients, C_S, C_{CE}, C_{CU} and C_{CI}, arises firstly from the explicit κ dependence in equations (A.2*b*) and (A.3) and secondly from the energy dependence of the real aberration coefficients themselves. It has been shown that the spherical and chromatic aberration coefficients for the homogeneous electric field produced by a planar electrode with on-axis pinhole opening (which mimics the hole in real objective lenses) are, to a good approximation, given by $C_{\mathrm{S}0} = C_{CE0} = l/\kappa$ in the limit of large κ, where l is the distance between sample and electrode [16]. Similar scaling relationships should also hold for the magnetic objective, which combines a focusing magnetic field with an electrode that approximates the homogeneous field. Therefore, we write $C_{\mathrm{S}0} = l_{\mathrm{eff,S}}/\kappa$ and $C_{CE0} = l_{\mathrm{eff,C}}/\kappa$, where the l_eff are the effective distances in the magnetic objective lens. The effective lengths $l_{\mathrm{eff,S}} = 7.2$ mm and $l_{\mathrm{eff,C}} = 3.3$ mm are determined from the calculated values of the real aberration coefficients $C_{\mathrm{S}0}$ and C_{CE0} in table A.1 and $\kappa = 5.55 \times 10^{-4}$ at $U_0 = 10$ eV and $U = 18$ keV. The difference

between the effective lengths may be related to the facts that the focusing magnetic field is located further than the electrode from the sample in the magnetic lens, and that these two lens elements contribute differently to the aberration coefficients. Apparently, the magnetic field contributes more to spherical aberrations than to chromatic. This is consistent with the stronger energy dependence of the spherical aberration contribution to resolution in a magnetic objective compared to the homogeneous field [17]. The model calculations that are presented in section 3 for $U_0 = 10$ eV confirm that the effects of voltage and current instabilities are negligible compared to the other factors, as expected by microscope design considerations.

References

[1] Recknagel A 1943 *Z. Phys.* **120** 331
[2] Bauer E 1994 *Rep. Prog. Phys.* **57** 895
[3] Chung W F and Altman M S 1998 *Ultramicroscopy* **74** 237
[4] Altman M S, Chung W F and Liu C H 1998 *Surf. Rev. Lett.* **5** 1143
[5] Müller Th 1995 *Diplomarbeit* Technische Universität Clausthal
[6] Born M and Wolf W 1999 *Principles of Optics* 7th edn (Cambridge: Cambridge University Press)
[7] Horiuchi S 1994 *Fundamentals of High Resolution Transmission Electron Microscopy* (Amsterdam: North-Holland) chapter 7
[8] Spence J C H 2003 *High Resolution Electron Microscopy* (Oxford: Oxford University Press) chapters 3 and 4
[9] Scherzer O 1943 *J. Appl. Phys.* **20** 20
[10] Frank J 1973 *Optik* **38** 519
[11] Wade R H and Frank J 1977 *Optik* **49** 81
[12] Hanßen K J and Trepte L 1971 *Optik* **32** 519
[13] Bauer E 1985 *Ultramicroscopy* **17** 51
[14] Schmidt Th *et al* 2002 *Surf. Rev. Lett.* **9** 223
[15] Adamec P 1994 private communication
[16] Lenc M and Müllerová I 1992 *Ultramicroscopy* **41** 411
[17] Chmelik J, Veneklasen L and Marx G 1989 *Optik* **83** 155